Eur. Phys. J. A (2021) 57:92
https://doi.org/10.1140/epja/s10050-021-00411-0

THE EUROPEAN
PHYSICAL JOURNAL A

Regular Article - Experimental Physics

# Experiments with A = 6–8 exotic beams in RIBRAS

**R. Lichtenthäler**[1,a], **O. C. B. Santos**[1], **A. Serra**[1], **U. Umbelino**[1], **K. C. C. Pires**[1], **J. R. B. Oliveira**[1], **A. Lépine-Szily**[1], **P. N. de Faria**[3], **V. Morcelle**[2]

[1] Instituto de Física, Universidade de São Paulo, São Paulo 05508-090, Brazil
[2] Universidade Federal Rural do Rio de Janeiro, Seropédica, RJ, Brazil
[3] Departamento de Física, Universidade Federal Fluminense do Rio de Janeiro, Rio de Janeiro 24210-310, Brazil

Received: 24 December 2020 / Accepted: 26 February 2021 / Published online: 12 March 2021

Communicated by Nicolas Alamanos

**Abstract** Experiments with secondary radioactive beams $^6$He, $^7$Be, $^8$Li and $^8$B on several targets have been performed in recent years at the Radioactive Ion Beams facility in Brasil (RIBRAS). We present results of elastic scattering and reaction measurements performed with this facility. A preliminary Coulomb excitation experiment using gamma-particle coincidence technique is described.

## 1 Introduction

Interest in low energy reactions has been revived over the last decades by the increasing use of radioactive ion beams (RIB). Light mass nuclei such as helium, lithium, berilium, boron have unstable bound isotopes which present interesting features such as the nuclear halo and cluster structures. Such features manifest in low energy scattering as an enhancement in the total reaction cross section and a strong coupling between different reaction channels. The Radioactive Ion Beams in Brasil (RIBRAS) facility [1–3] includes a double solenoid system which has been operating since 2004 in the Nuclear Physics Open Laboratory (LAFN) of the University of Sao Paulo delivering secondary beams of light exotic nuclei such as $^6$He, $^8$Li, $^7$Be, $^8$B among others. The 8UD-Pelletron produces primary beams of stable isotopes of energies in the range 3-5 MeV/nucleon.

Several studies involving elastic scattering and reactions induced by exotic projectiles have been performed in RIBRAS since 2004 [4–12]. By using different mass targets we are able to study the interplay between Coulomb and nuclear forces in the scattering process. For light projectile/targets ($A \leq 12$), the Coulomb barrier is small and one can go several times above the Coulomb barrier. In this regime, there is a large projectile-target matter overlap and the strong nuclear interaction dominates, with the opening of a large number of reaction channels such as fusion, transfers and breakup. As we move towards intermediate mass ($12 \leq A \leq 80$) to heavier targets ($A > 80$), the Coulomb barrier becomes more important, increasing the closest approach distance and reducing the projectile-target overlap. As a consequence, reaction channels are closed and processes such as elastic, inelastic scattering, Coulomb breakup and Coulomb excitation (Coulex) become relatively more important. The use of different mass targets and projectiles allows the study of the behavior of the elastic scattering and the total reaction cross sections for different energy over Coulomb barrier ratios.

In this paper, we present experimental data of the collision of $^6$He, $^7$Be, $^8$B and $^8$Li beams on $^9$Be, $^{58}$Ni and $^{120}$Sn targets, previously reported [6,8,11,13,14]. In Sect. 2, we describe the RIBRAS system and some characteristics of $^8$B, $^7$Be and $^8$Li secondary beams. In Sect. 3, we present results of $^6$He, $^7$Be, $^8$B and $^8$Li scattering. The elastic scattering angular distributions have been analysed by Optical Model, three and four-body Continuum Discretized Coupled Channels (CDCC) calculations which are, currently, the state of the art in terms of theoretical analysis. In Sect. 4, we present data of reaction channels other than elastic scattering and discuss the effect of neutron transfer/breakup in low energy reactions induced by radioactive projectiles. In our last review [3] we foresaw the installation of a gamma-particle detection system in RIBRAS. In Sect. 4.2, we present the results of the first experiment of gamma-particle coincidence performed in RIBRAS. A Coulomb excitation experiment is described and some preliminary results are presented. Finally, in the last section, we summarize the results and present the conclusions.

---

[a] e-mail: rubens@if.usp.br (corresponding author)

## 2 The RIBRAS system

The Radioactive Ion Beams in Brasil (RIBRAS) system consists of two superconducting solenoids used to select and focus the secondary particles of radioactive nuclei produced in the collision between a primary beam, delivered by the 8UD-Pelletron accelerator of the University of Sao Paulo (USP), and a primary target. The system is installed in the 45B beam line of the LAFN of the Nuclear Physics department of the Physics Institute of USP. The original project to fund the purchase of the RIBRAS system and its installation was proposed by Mahir Saleh Hussein, who was the head of the Nuclear Physics Department in 1997. Hussein's idea was to open a new experimental research line for radioactive ion beams (RIB) in Brazil. At that time, RIB was the new frontier of research in low/intermediate energy nuclear physics and by 1985–1990 several laboratories all over the world were installing facilities to produce secondary beams of exotic nuclei. Most RIB facilities operated at intermediate energies (20 MeV/nucleon–1 GeV/nucleon) and only a few laboratories were able to produce low energy secondary beams, RIBRAS being the first in the southern hemisphere.

The two RIBRAS superconducting solenoids (see Fig. 1) operate in line and produce a maximum field of B = 6.5 T each (at I = 90 A) and a field integral of 5.0 T.m in a 30 cm diameter 1m long bore. The superconducting magnets are stored in 1 m ×1 m cylindrical cryostats inside a 300 l liquid helium vessel surrounded by a 180 l liquid nitrogen cover to minimize liquid helium evaporation.

The secondary beam is produced by the in-flight method, and the main components of the beam line are shown in Fig. 1: the primary target chamber (chamber 1), Faraday cup, first solenoid, central scattering chamber (chamber 2), second solenoid and scattering chamber 3. The secondary particles produced by nuclear reactions in chamber 1 enter the angular acceptance of the first solenoid ($2^\circ \leq \theta \leq 6^\circ$) and are focused in scattering chamber 2 in different positions, according to their magnetic rigidity up to a maximum $B\rho = 2$ T.m. The primary target is a gas cell of 2.3 cm length with two havar windows. The exit window can be replaced by a $^9$Be foil, which is the standard target for the $^6$He and $^8$Li beams production. The Faraday cup is there for both, to stop and measure the primary beam intensity. The Faraday cup current is integrated providing a measurement of the total number of primary beam particles incident in the primary target during the experiment. Collimators and blockers are placed in strategic positions to block unwanted secondary particles. Nevertheless, the secondary beam in chamber 2 is still contaminated by degraded primary beam particles in addition to other light particles such as protons, deuterons, tritons and alpha-particles produced in the primary target. An additional selection is possible by placing an absorber in the central chamber and using the second solenoid to reselect and focus the secondary beam of interest on chamber 3, which improves its purity to about $92-97\%$ in some cases. Experiments have been performed either in chamber 2 or in chamber 3 depending on the required secondary beam purity.

The secondary beams are produced by nucleon transfer reactions between the primary beam and primary target. Usual primary beams are $^{6,7}$Li, $^{10,11}$B, $^{12,13}$C among others, and the most common primary targets are $^9$Be, LiF and an $^3$He gas cell. In Table 1, we present some of the secondary beams produced so far by RIBRAS.

The standard detection system consists of silicon detector $\Delta$E-E telescopes to identify and measure the energy of the scattered particles. Thin $\Delta$E detectors of $25-50$ μm and $150-300$ mm$^2$ area followed by thicker E detectors of $150-1000$ μm permit identification of most of the light particles produced in the secondary reactions. In Fig. 2, we show two-dimensional $\Delta$E–E spectra obtained in chamber 2 with $^{58}$Ni and gold secondary targets. The $^8$Li secondary beam was produced by the reaction reported in Table 1.

Scattering measurements at forward angles with gold targets provide the secondary beam intensity and also its contaminants since the scattering on the gold target at RIBRAS energies is pure Rutherford and almost no reactions are expected to occur. In Fig. 2b, we clearly see the light contaminants $p, d, t, \alpha$ and $^6$He well separated from the $^8$Li peak. On the other hand, the spectrum with $^{58}$Ni target shown in Fig. 2a presents a large yield of $^7$Li produced in reactions, in addition to the contaminants of the secondary beam. We see that our mass resolution is sufficient to clearly separate the $^{7,8}$Li isotopes.

In Fig. 3, we show a spectrum of the $^8$B beam scattered in a Gold target. The $^8$B beam was produced by the $^3$He($^6$Li,$^8$B) reaction using a gas cell primary target (see Table 1) and this is the only known reaction to produce a $^8$B beam at these low energies. The $^8$B peak is well separated from the other (more intense) $^7$Be, $^6$Li and $^{3,4}$He contaminants. The $^8$B secondary beam intensities are in the range of $10^{3-4}$ pps.

The secondary beam energy resolution has been measured for each secondary beam and is very much dependent on the production reaction varying from 470 keV for $^8$Li up to 1 MeV for $^6$He or $>$ 1 MeV for $^8$B. Straggling in the primary target and the reaction kinematics within the solenoid acceptance are the main factors that determine the secondary beam energy resolution.

All the measurements in RIBRAS have been performed using a gold target to normalize the data. Scattering in gold target is pure Rutherford for almost all angles and energies of the experiments, providing a way to normalize the cross sections by comparing adjacent gold target runs performed before and after each run with the target of interest. This method of normalization cancels out the detectors solid angles dependence and depends only on the ratio of the secondary beam intensities in adjacent runs. This ratio is taken

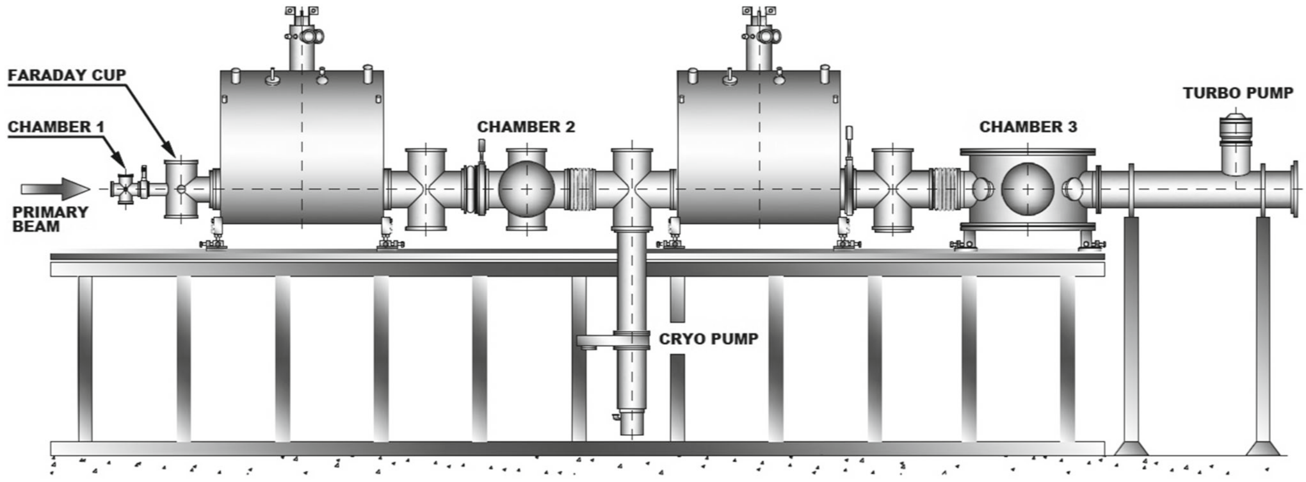

**Fig. 1** RIBRAS system installed in the 45B Pelletron beam line

**Table 1** Secondary beams produced at the RIBRAS, nuclear reactions used for their production and the intensities, reported in *pps* per 1μA of primary beam

| Secondary beam | Production reaction | Intensity (pps) |
|---|---|---|
| $^{8}$Li | $^{9}$Be($^{7}$Li,$^{8}$Li)$^{8}$Be | $10^{5}$–$10^{6}$ |
| $^{6}$He | $^{9}$Be($^{7}$Li,$^{6}$He)$^{10}$B | $10^{4}$–$10^{5}$ |
| $^{7}$Be | $^{3}$He($^{6}$Li,$^{7}$Be)d | $10^{4}$–$10^{5}$ |
| $^{7}$Be | $^{7}$Li($^{6}$Li,$^{7}$Be)$^{6}$He | $10^{4}$–$10^{5}$ |
| $^{8}$B | $^{3}$He($^{6}$Li,$^{8}$B)n | $10^{3-4}$ |
| $^{10}$Be | $^{9}$Be($^{11}$B,$^{10}$Be)$^{10}$B | $10^{5}$ |
| $^{12}$B | $^{9}$Be($^{11}$B,$^{12}$B)$^{8}$Be | $10^{5}$ |

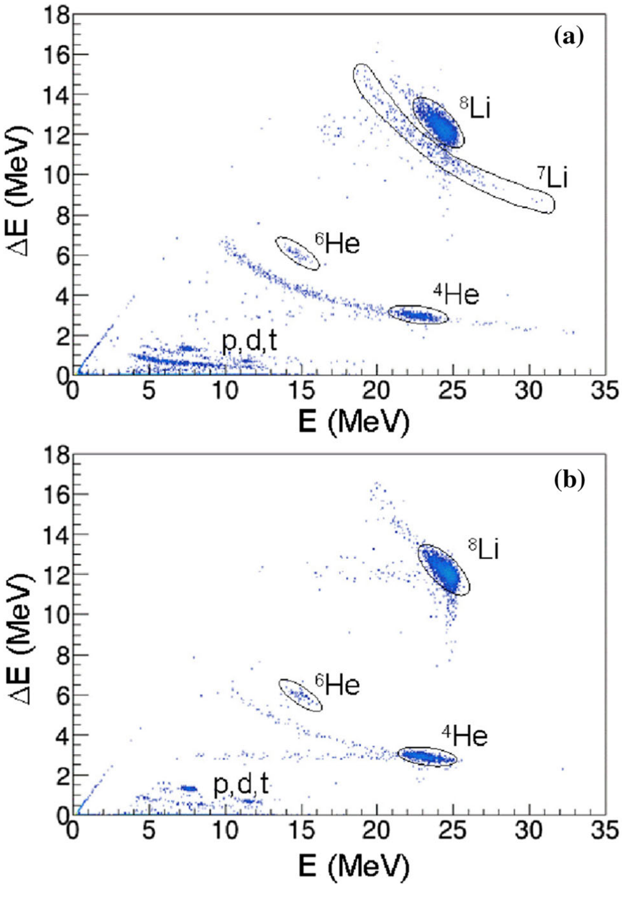

**Fig. 2** Two-dimensional $\Delta$E-E spectra obtained with **a** $^{58}$Ni and **b** gold targets at $\theta_{\mathrm{lab}}$ = 32° and E$_{\mathrm{lab}}$=26.1 MeV. Figure taken from [15]

as equal to the integrated primary beam ratios, obtained from the integrated Faraday cup current. This method provides an absolute normalization of the angular distributions and no additional normalization is done.

Among other similar low energy facilities which are in operation in the world, we mention the Notre Dame University (EUA) TwinSol [17] facility, the CRIB at RIKEN [18] in Toquio and EXOTIC at Legnaro (Italy), [19–22], among others. RIBRAS is very similar to the TwinSol system and its installation in Sao Paulo was indeed firstly suggested by J. Kolata to M. Hussein during a workshop held in São Paulo in 1997. The idea was to install RIBRAS after the 10 MV LINAC pos-accelerator, which was under construction in the Sao Paulo Nuclear Physics department. As the RIBRAS system was completed before the LINAC, a decision was taken to first install RIBRAS in one of the 8UD-Pelletron accelerator beam lines (45B). Very similar secondary beams and intensities are available in RIBRAS, TwinSol and EXOTIC facilities. The Legnaro-EXOTIC facility uses a different optical system with a dipole, quadrupoles and a Wien filter in line to select the secondary beam. Other ISOL (Isotopic on-Line) facilities using higher energy driver accelerators are in operation in the world which are capable of producing low energy secondary beams of light exotic nuclei farther from the stability valley such as $^{11}$Li, $^{11}$Be and others [23–27].

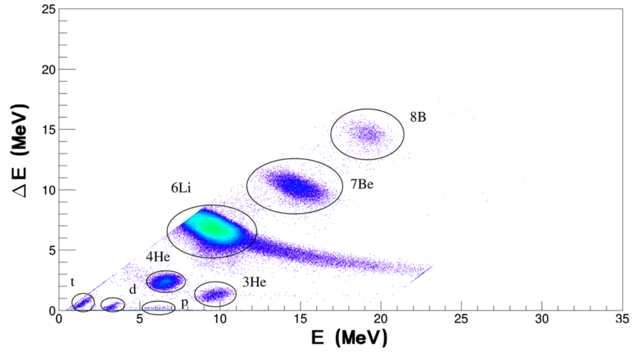

**Fig. 3** Two-dimensional $\Delta$E-E spectrum obtained with $^8$B beam on a gold target at $\theta_{\text{lab}}$ = 12° and E$_{\text{lab}}$ = 25.8 MeV. Figure taken from [16]

## 3 Elastic scattering of A = 6–8 nuclei

Helium-6 and lithium-8 were the first secondary beams produced in RIBRAS during its inauguration in the XIII Swieca Summer School on experimental physics held in São Paulo in 2004. The $^6$He and $^8$Li secondary beams have been produced by proton pickup and neutron stripping $^7$Li+$^9$Be reaction (see Table 1). Helium-6 presents a $\alpha + n + n$ structure bound by 0.973 MeV with $\beta^-$ decay half-life of 806.7 ms [28]. The $\alpha$ particle and the two neutrons in helium-6 form a three-body Borromean nucleus which is bound only if the three components are present. No two-body subsystems are bound and the two weakly bound neutrons form an extended nuclear halo around the $\alpha$ core which increases the nuclear radius. As a consequence, the total reaction cross-section of systems with a $^6$He projectile are larger when compared to similar mass stable systems as will be shown further in this section.

All the experiments reported in the next subsections were performed in scattering chamber 2 (Fig. 1). The purity of the secondary beams in scattering chamber 2 are poor, ranging from 2–4 % in the case of the proton rich nuclei $^7$Be and $^8$B up to 16% and 44% in the case of the neutron rich $^6$He and $^8$Li, respectively [3]. In scattering chamber 3, the purity is very much improved to values above 90% for the neutron rich $^6$He and $^8$Li beams.

### 3.1 $^6$He+$^9$Be scattering

The $^6$He+$^9$Be measurement has been performed in scattering chamber 2 of the RIBRAS facility. The $^6$He secondary beam was produced by the $^9$Be($^7$Li,$^6$He)$^{10}$B reaction with a 12-$\mu m$ $^9$Be foil and a 200−nAe $^7$Li primary beam of 22.18 and 26.10 MeV. A tungsten Faraday cup to stop the primary beam and measure its current during the experiment. In those conditions, the $^6$He average secondary beam intensity was of about $10^4$ pps.

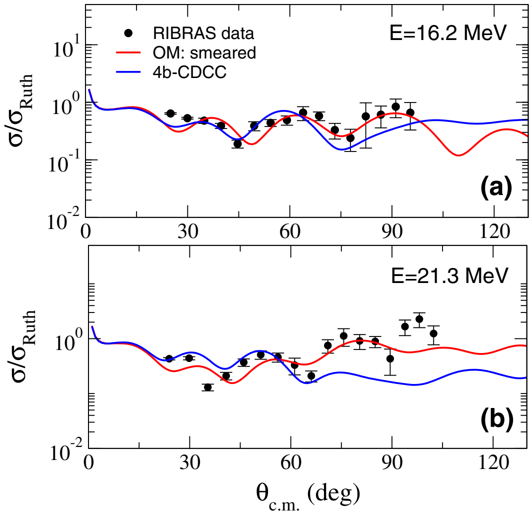

**Fig. 4** Elastic scattering angular distributions of the $^6$He+$^9$Be system [11]. Figure taken from refs. [11,12]

**Table 2** Parameters of the optical model calculations

| $E_{\text{lab}}$ (MeV) | Potencial | $V_0$ (MeV) | $r_0$ (fm) | $a_0$ (fm) | $W_0$ (MeV) | $r_i$ (fm) | $a_i$ (fm) |
|---|---|---|---|---|---|---|---|
| 16.2 | 2n+$^9$Be | 61.01 | 1.51 | 0.55 | 20.00 | 1.20 | 1.01 |
| 21.3 | 2n+$^9$Be | 21.41 | 1.51 | 0.54 | 10.02 | 1.35 | 1.56 |

In Fig. 4, we show two $^6$He+$^9$Be angular distributions measured at RIBRAS and analysed by optical model and four-body CDCC (Continuuum Discretized Coupled Channels) calculations [11,29–31]. For this light system, we can go 8–10 times above the system Coulomb barrier ($V_{cb}^{lab} = 2.0$ MeV)[1] and the angular distributions present a typical Fraunhofer diffractive pattern with oscillations, whose angular period is related to the inverse of the grazing angular momentum. The analysis corresponds to a four-body CDCC (blue color) [11] calculation using optical potentials for the $\alpha$+$^9$Be and $n$+$^9$Be given in refs. [33,34] and an optical model fit (red color). In the latter, the interaction between the projectile $^6$He and the $^9$Be target has been calculated in the cluster-folding model, separated into two contributions, one for the alpha-target (core), taken from Ref. [35], and another for the di-neutron-target (halo) taken in a Woods–Saxon (WS) shape. Only the di-neutron-target (halo) part has been adjusted to fit the data, resulting in a long-range diffuseness in the imaginary part of the WS potential shown in Table 2 [12].

In Fig. 5, we compare the total reaction cross sections obtained from these analyses with systems of similar masses in a reduced plot. The reduced cross sections and energies were obtained from the expressions below [36]:

---

[1] All Coulomb barriers have been calculated using the formula given in Refs. [10,32].

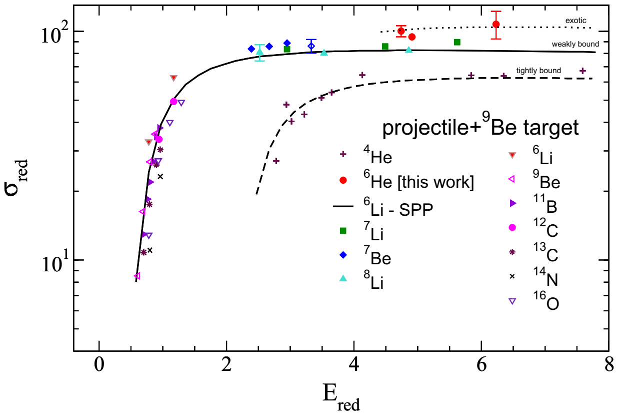

**Fig. 5** Total reaction cross-section for several projectiles on $^9$Be target. The total reaction cross sections for different projectiles can be found in Ref. [12] and references therein. Solid line is an optical model calculation using Sao Paulo optical potential [37]. Dashed and dotted lines are a guide to the eyes. This figure is based on the results of Ref. [12]

$$\sigma_{red} = \frac{\sigma_{exp}}{(A_1^{1/3} + A_2^{1/3})^2} \tag{1}$$

$$E_{red} = \frac{E_{cm}(A_1^{1/3} + A_2^{1/3})}{Z_1 Z_2} \tag{2}$$

In the expressions given above $A_i$ and $Z_i$ stand for the masses and atomic numbers of the projectile and target and $\sigma_{exp}$ is the total reaction cross section obtained from the fit. We observe a large enhancement of the $^6$He cross sections compared to the $^4$He core. Compared to the light weakly bound neighbour systems, there is a smaller but still significant enhancement of 15–25 % which is attributed to the $^6$He halo effect. This effect will be amplified for heavier targets as we will show in the next subsections.

### 3.2 $^7$Be+$^9$Be elastic transfer

The $^7$Be+$^9$Be quasi-elastic scattering was measured at RIBRAS with a 23.1 MeV ($V_{cb}^{lab} = 4.6$ MeV). The $^7$Be beam was produced by the LiF($^6$Li,$^7$Be) reaction with lithium-fluorine primary target. During the experiment, the $^7$Be secondary beam intensity was of the order of $5 \times 10^4$ pps. These results were first reported in Ref. [13].

In Fig. 6, we show a bi-parametric $\Delta$E-E spectrum of the scattered secondary beam on the $^9$Be target. We see the $^7$Be peak well separated from the $^{6,7}$Li, $^4$He and light particles contaminants. In addition, there are a few counts above the $^7$Be elastic peak (see Fig. 6). Those events correspond to $^9$Be particles detected at forward angles which come either from back scattered target particles or from a $^7$Be two-neutron pick-up reaction. In Fig. 7, we present the cross sections. The forward angles correspond to the $^7$Be particles and the four points at backward angles correspond to the $^9$Be events detected at forward angles in the laboratory. The observed backward cross sections of about 1 mb are in the lower limit of the RIBRAS sensitivity. The observed events are in the $^9$Be line and have the correct energy. This is confirmed by rigorous energy calibrations of the $E$ and $\Delta E$ detectors so that they can not be confused with $^{10}$B events coming from the $^9$Be($^7$Be, $^6$Li)$^{10}$B reaction [38].

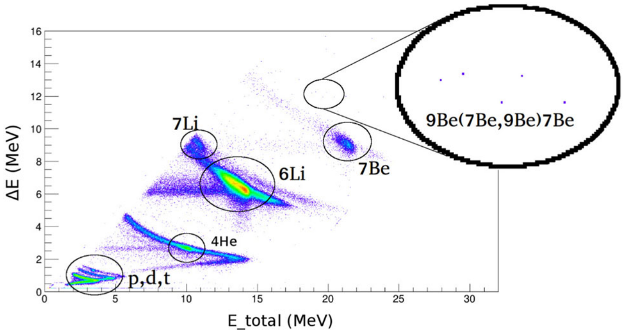

**Fig. 6** Two-dimensional $\Delta$E-E spectrum obtained with $^7$Be beam on $^9$Be target at $\theta_{cm}$=15° and $E_{lab}$=23.1 MeV. Figure taken from Ref. [13]

The observed $^9$Be cross sections at backward angles were orders of magnitude larger than optical model predictions, indicating that processes other than pure elastic scattering are taking place at backward angles. The $^9$Be($^7$Be,$^9$Be) elastic transfer reaction is the candidate to explain this backward rise. In Fig. 7, we present the results of Coupled Reaction Channels (CRC) calculations considering the coupling to the two-neutron transfer channel. In those CRC calculations, the scattering amplitudes for the elastic transfer process have been added to the elastic scattering ($f(\theta) + S_f f_t(\pi - \theta)$) to explain the backward angles effect. IC stands for the independent coordinate model used to describe the two-neutron transfer [39]. The São Paulo double folding potential [37] was used in both real and imaginary parts of the optical potentials of the entrance and outgoing partitions. In the entrance partition, a strength factor 0.6 was used for both real and imaginary parts. The use of this factor is justified as taking into account the missing couplings to dissipative processes [40], as well as, for the coupling to the continuum states that were not explicitly included in the coupling scheme.

Shell model calculated spectroscopic factors, $S_f$, were used to normalize the transfer amplitudes. The results show that the observed yields can be explained by the effect of the two-neutron elastic transfer reaction on the elastic scattering. Calculations have been performed using two types of optical potentials (bare), a Woods-Saxon (WS) adjusted to fit the forward angles and a double folding Sao Paulo potential (SPP) [37]. The WS provides a very good fit at forward angles but underestimates the backward cross sections whereas de SPP reproduces the backward angles but do not fit very well the forward angles showing that the results depend on the optical potential choice.

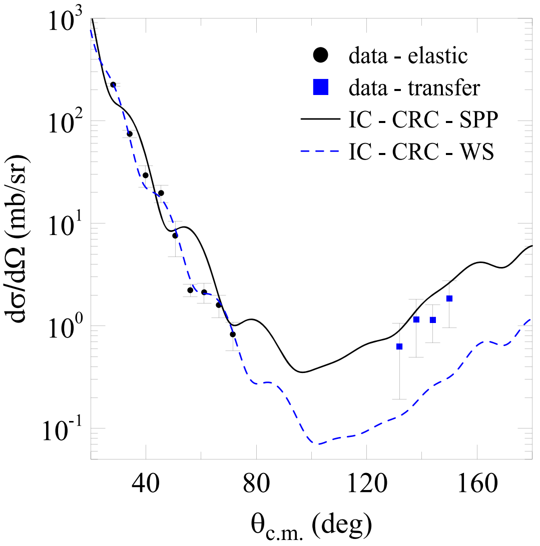

**Fig. 7** Elastic scattering angular distribution of the $^7$Be $+^9$ Be system [13]. The forward angles data correspond to events detected via $^7$Be and the backward correspond to events detected via $^9$Be, all detected at forward laboratory angles. Figure taken from Ref. [13]

### 3.3 $^6$He $+^{58}$ Ni scattering

The experiment was performed in the scattering chamber 2 of the RIBRAS system. A $^7$Li$^{3+}$ primary beam of energies $E_{\text{lab}} = 18.0$, 22.0, and 27.0 MeV and intensity of $I \approx 200$ nAe was used to produce the $^6$He$^{2+}$ secondary beam by the $^9$Be($^7$Li,$^6$ He)$^{10}$B reaction. A 12 μm $^9$Be foil was used as primary target and an average secondary beam intensity of about $10^5$ pps was measured.

In Fig. 8, we present $^6$He $+^{58}$ Ni angular distributions at 12.2, 16.5 and 21.7 MeV in the laboratory ($V_{cb}^{lab} = 8.7$ MeV). These results have been first reported in Ref. [14]. The angular distributions have been analysed by 3b- and 4b-CDCC calculations. We see that the calculated angular distributions present a different diffraction pattern with a pronounced Fresnel peak at forward angles and an exponential decrease of the cross section for backward angles. The data, on the other hand, present an increase of the cross sections at backward angles when compared to the no-coupling calculations (dotted line). The 4b-CDCC calculation nicely reproduces these features without any parameter adjustment (blue line) whereas three-body CDCC accounts for only a part of the overall effect. No parameter variation was done in these calculations. In Table 3, we present the optical potentials used in the 4b-CDCC calculations.

In Fig. 10, we plot the reduced total reaction cross sections for A = 60 systems including the $^6$He $+^{58}$ Ni data. The following formulas were used for the reduced quantities: $\sigma_{red} = \sigma_{exp}/\pi R_b^2$ and $E_{red} = E_{cm}/Vcb$ where $V_{cb}$ and $R_b$ were obtained using the formulas given in Refs. [10,32]. Note that, since the formulas from Ref. [10,32] provide realistic values of $V_{cb}$ and $R_b$, the reduced cross sections are all below unity tending to one as the energy increases and $E_{red} = 1$ stands for the real Coulomb barrier position, differently from the reduction used in subsection 3.1. Again, we see three classes of reduced cross sections increasing from tightly bound to weakly bound and finally to the $^6$He halo projectile.

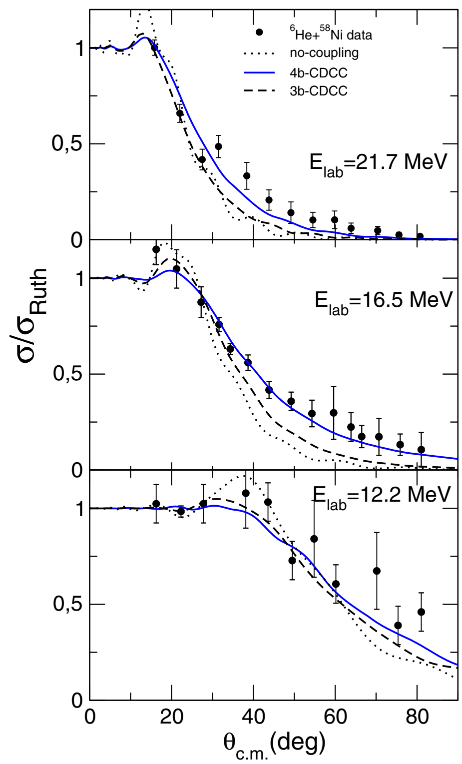

**Fig. 8** Elastic scattering angular distributions of the $^6$He$+^{58}$Ni system. Figure taken from Ref. [14]

### 3.4 $^6$He $+^{120}$ Sn scattering

Four $^6$He$+^{120}$Sn elastic angular distributions were measured at 17.4, 18.05, 19.8 and 20.5 MeV ($V_{cb}^{lab} = 13.3$ MeV). During the experiment the $^6$He beam intensities were around $10^4 - -10^5$ pps at the secondary-target position in scattering chamber 2.

These results were first reported in Ref. [6] and are shown in Fig. 9. The data have been analysed by Optical model, 3b and 4b-CDCC calculations and the total reaction cross sections have been obtained. The $^6$He$-^{120}$Sn diagonal potential was calculated in the cluster-folding method using fragment-target interactions represented by optical potentials that reproduce the elastic scatterings at the corresponding energies. The $n-^{120}$Sn potential was taken from the global parametrization of Koning and Delaroche [43] and the $\alpha-^{120}$ Sn potential was from the global parametrization of Avrigeanu et al. [44].

**Table 3** Optical potentials used in the CDCC calculations at the three energies, respectively, for $\alpha$+$^{58}$Ni (top row) and $n$+$^{58}$Ni (bottom row). Table taken from Ref. [14]

| $E_{\text{lab}}$ (MeV) | $V_0$ (MeV) | $r_0$ (fm) | $a_0$ (fm) | $W_0$ (MeV) | $r_i$ (fm) | $a_i$ (fm) | $W_d$ (MeV) | $r_d$ (fm) | $a_d$ (fm) | References |
|---|---|---|---|---|---|---|---|---|---|---|
| 12.2 | 60.00 | 1.62 | 0.54 | 0.50 | 1.62 | 0.54 | 15.84 | 1.52 | 0.44 | [41] |
| | 61.36 | 1.45 | 0.57 | – | – | – | 1.28 | 1.45 | 0.50 | [42] |
| 16.5 | 165.90 | 1.62 | 0.40 | 11.40 | 1.62 | 0.4 | 23.98 | 1.52 | 0.44 | [35] |
| | 42.00 | 1.46 | 0.35 | 6.09 | 1.46 | 0.35 | – | – | – | [35] |
| 21.7 | 135.10 | 1.35 | 0.64 | 7.64 | 1.34 | 0.50 | 18.97 | 1.52 | 0.44 | [35] |
| | 42.00 | 1.46 | 0.35 | 6.09 | 1.46 | 0.35 | – | – | – | [35] |

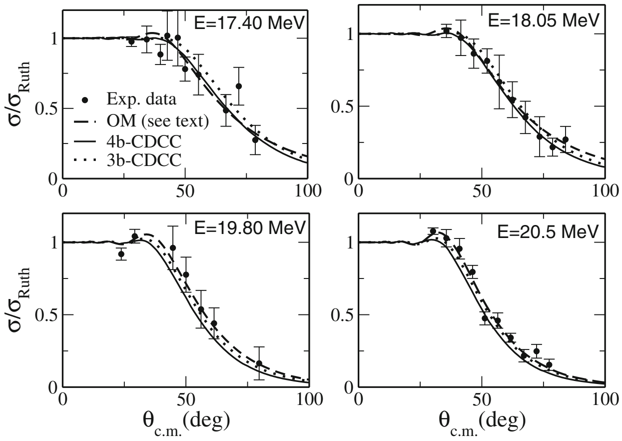

**Fig. 9** Elastic scattering angular distributions of the $^{6}$He +$^{120}$ Sn system [6]. Figure taken from Ref. [6]

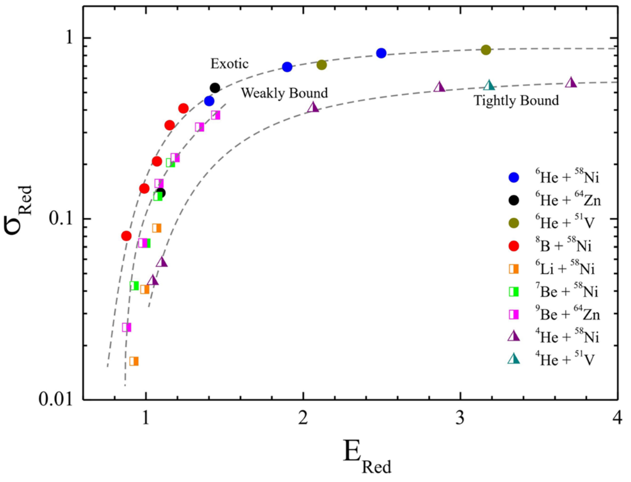

**Fig. 10** Reduced total reaction cross-section for systems with target mass around A = 60. Dashed lines are guidelines. This Figure is based on the results presented in Ref. [3]

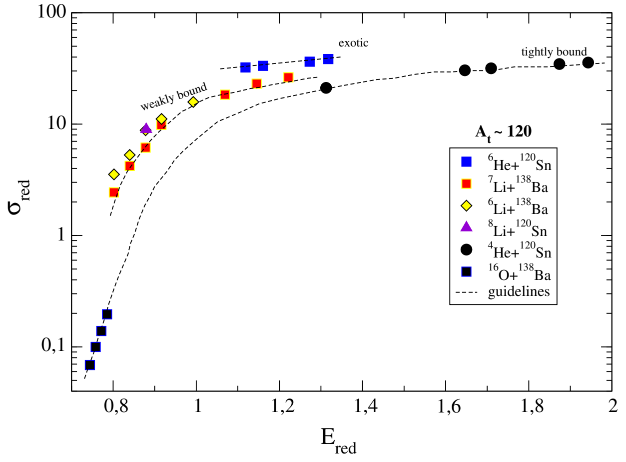

**Fig. 11** Reduced total reaction cross-section compared to systems with target mass around A = 120 [6]. Dashed lines are guidelines. This Figure based on the results of Ref. [6]

The 3b- and 4b-CDCC calculations have reproduced quite well the data considering the experimental error bars. As seen previously, a comparison of the $^{6}$He +$^{120}$ Sn total reaction cross section with weakly and strongly bound projectiles is presented in Fig. 11 using the same reduction as in Sect. 3.1. The results show three classes of reduced cross sections, increasing from strongly bound to weakly bound and finally the exotic $^{6}$He projectile. The reaction channels contributing to this enhancement will be investigated in Sect. 4.

### 3.5 $^{8}$B+$^{27}$Al scattering

$^{8}$B is one of the most exotic nuclei in the proton rich side of the nuclear chart. Its p+$^{7}$Be breakup energy of only 0.138 MeV is the lowest binding energy in the light nuclei region what makes it a proton halo candidate. The $^{8}$B secondary beam is produced by the $^{3}$He($^{6}$Li,$^{8}$B) reaction using a gas cell at 1 atm $^{3}$He pressure and 2.2 µm havar windows. The primary target was bombarded with a 300 $nAe$, 26.5 MeV $^{6}$Li beam producing a $^{8}$B beam of $10^{3-4}$ pps in the secondary target position (chamber 2).

In Fig. 3, we see that the contaminants of the $^{8}$B beam are intense but well separated in energy. The most intense contaminant is $^{6}$Li from the primary beam particles scattered in the havar foils of the gas cell. There are also $^{7}$Be and lighter particles such as alphas $^{3}$He, protons, deuterons and tritons. If we project the $\Delta$E–E spectrum in the total energy axis, we see the $^{6}$Li, $^{7}$Be and $^{8}$B peaks well separated (see Fig. 12). Telescopes are mounted at forward angles to pro-

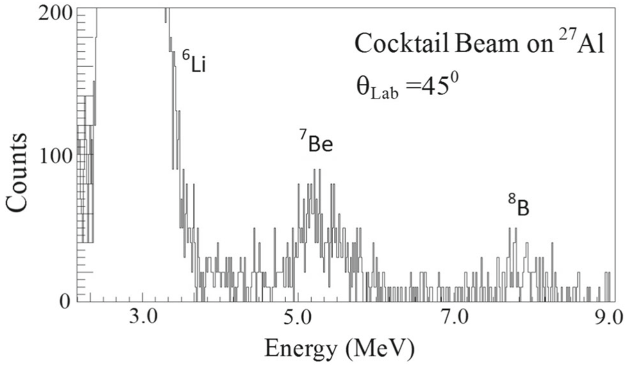

**Fig. 12** Monoparametric spectrum of the $^8$B+$^{27}$Al collision. Figure based on results from Ref. [8]

vide a identification of the $^8$B secondary beam. At backward angles, the $^8$B particles usually do not have enough energy to punch through the 25 μm $\Delta$E detectors but, nevertheless, it is possible to measure $^8$B and $^7$Be scattering by using single energy detectors due to the good separation in energy of the contaminants.

Two $^8$B+$^{27}$Al angular distributions at 15.3 and 21.7 MeV ($V_{cb}^{lab} = 13.4$ MeV) are presented in Fig. 13. These data have been measured in two different experiments, one performed at RIBRAS (15.3 MeV) and another in TwinSol (21.7 MeV) [17]. In the RIBRAS experiment, we used one telescope at forward angles for particles identification and two single E detectors at backward angles. In the TwinSol experiment at 21.7 MeV, four large area (23 mm × 23 mm) X–Y position sensitive detectors were used to cover the angular range from 20° to 55°. The analysis of these data was performed by dividing the PSD detectors (x signal) into two halves (due to the very low statistics), so only two angles per detector were obtained. A blocker was placed on the forward half of the more frontal PSD detector to avoid direct impingement of the beam on it.

Optical model and CDCC calculations have been performed. A Woods-Saxon potential was used in the optical model calculations whose geometry was fixed ($r_{r,i} = 1.3$ fm and $a_{r,i} = 0.65$ fm) and only the strengths $V_0$ and $W_0$ of the real and imaginary parts were varied to best fit the angular distributions. The resulting parameters are shown in Table 4.

The CDCC calculation and coupling to the p+$^7$Be breakup channel also provide a good description of the data. The standard Sao Paulo potential [37] was used for both fragment-target interactions, $p$–$^{27}$Al and $^7$Be-$^{27}$Al, with strength coefficients N$_r$ = 1.0 and N$_i$ = 0.78, respectively for real and imaginary potentials.

The total reaction cross sections for several projectiles on $^{27}$Al target are shown in Fig. 14. In order to compare different projectiles, the cross sections have been reduced as described in Refs. [8,10,32] and in Sect. 3.3. This plot shows the increase in the total reaction cross section as we go from systems with strongly bound projectiles such as $^{16}$O to weakly bound stable and finally the exotic $^7$Be and $^8$B, the latter presenting the highest cross sections.

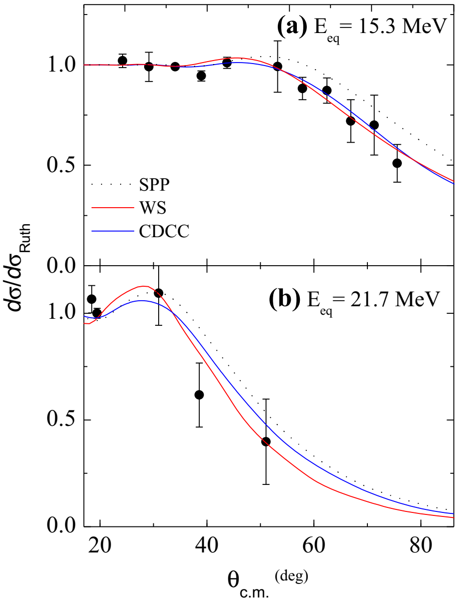

**Fig. 13** Elastic scattering angular distributions of the $^8$B+$^{27}$Al system. Figure taken from Ref. [8]

**Table 4** Parameters of the optical model fits and total reaction cross sections for the $^8$Be+$^{27}$Al system [8]

| $E_{\rm lab}$ (MeV) | $V_0$ (MeV) | $W_0$ (MeV) | $\sigma_R$ (mb) | $\chi^2/N$ | Setup |
|---|---|---|---|---|---|
| 15.3 | 21.7 | 29.6 | 506 | 0.31 | RIBRAS |
| 21.7 | 32.1 | . 16.0 | 1074 | 0.99 | TwinSol |

The total $^8$B+$^{27}$Al reaction cross section of 1074 mb at 21.7 MeV can be compared to the fusion cross section obtained from a similar system ($^8$B+$^{28}$Si) at a similar energy 20 MeV [45] and the fusion cross section of 553 mb exhausts about one-half of the total reaction cross section.

## 4 Beyond elastic scattering

In the previous sections we discussed the effects of the elastic breakup channel on elastic scattering angular distributions as described by Continuum Discretized Coupled Channel (CDCC) calculations. In the case of $^6$He projectile, the breakup into an alpha particle and two neutrons involves four particles in the final channel, requiring the use of four-body CDCC calculations to be described [25,30,31,46,47]. However, as we look to reaction channels other than the elastic scattering such as alpha-particle production in the case of $^6$He, we immediately see that CDCC is not able to explain

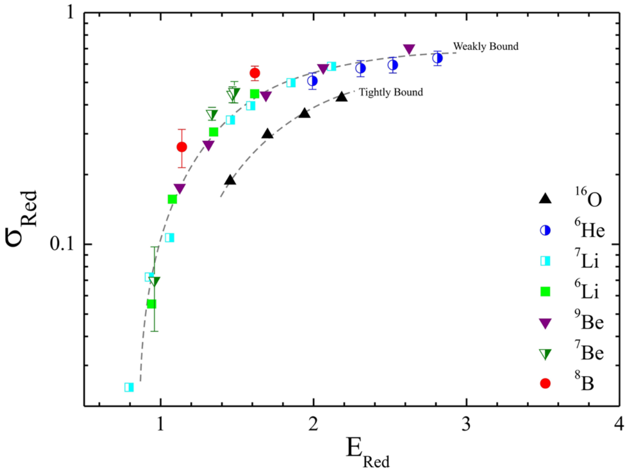

**Fig. 14** Reduced total reaction cross-sections of several projectiles on a $^{27}$Al target [8]. Dashed lines are guides to the eyes. Figure taken from Ref. [8]

the large yield of alpha particles seen in the two-dimensional spectra (see Fig. 15). The CDCC calculations predict breakup cross sections considerably smaller than the observations [48,49]. There are clear indications that reactions channels other than the direct breakup are contributing to the observed alpha particle yields [5,48]. Among those possible reactions, particle transfers to bound and excited states of the $^{120}$Sn target, incomplete fusion and non elastic breakup comprise a set of inclusive processes in which a particle or a fragment of the projectile is captured by the target, forming a highly excited recoil nucleus, which will subsequently decay by gammas and/or particles whereas the projectile fragment continues on to the detector.

In the next subsection, we will present some results of measurements of angular and energy distributions of $\alpha$-particles from $^{6}$He $+^{120}$ Sn collision performed in scattering chamber 3 (see Fig. 1). A preliminary particle-gamma coincidence experiment performed in scattering chamber 3 is reported in Sect. 4.2.

### 4.1 The $^{120}$Sn($^{6}$He,$\alpha$) reaction

The $^{6}$He $+^{120}$ Sn collision and the alpha-particle production were investigated as a function of the incident energy. Experiments have been performed in scattering chamber 2 and in scattering chamber 3 where the $^{6}$He secondary beam is more pure. A $10^{5}$ pps $^{6}$He average secondary beam was obtained during the experiments.

We performed measurements of the $^{120}$Sn($^{6}$He,$\alpha$)X reaction [5,48] at several energies (see Figs. 16 and 17). In Fig. 16 (left), we present the energy distributions of the alpha-particles as seen in the $\Delta$E–E spectrum (see Fig. 15). On the right, we transformed the energy axis to Q-value considering the kinematics of the two-neutron transfer reaction $^{120}$Sn($^{6}$He,$\alpha$)$^{122}$Sn. This transformation allows us to compare alpha-particle distributions measured at different angles. In this experiment, the alpha-particles were measured at angles around 60 deg in the laboratory, which is around the grazing angle as shown in Fig. 17. We see from Fig. 16 that the transfer reaction populates excited states of the $^{122}$Sn nucleus below and above $Q_{reac} = 0.0$ MeV covering a wide excitation energy range in the recoil $^{122}$Sn nucleus. Reaction Q-values go from values around zero at 17.4 MeV bombarding energy up to negative values around $-5.0$ MeV at 24.5 MeV. As the ground state Q-value for the 2n-transfer reaction is $+14.01$ MeV, the measured Q-values ($Q \leq 0$) correspond to a region from 13.5 to 19.5 MeV excitation energy in the recoil nucleus [48]. These excitation energies correspond to states in the $^{122}$Sn continuum, well above the 8.815 MeV 1n-threshold.

The alpha-particle angular distributions are shown in Fig. 17 for four incident energies [5]. The total (angle integrated) alpha-particle cross sections and estimated errors obtained from the DWBA curves from Fig. 17 are given as: 940(216), 1031(114), 977(293) and 1141(228) mb respectively for the energies 17.4, 18.05, 19.8 and 20.5 MeV.

In Fig. 18, we compare our results with data from the literature [50–55] for other stable and exotic systems. In order to compare different systems at different energies, the data are presented as a function of the ratio $E/V_{cb}$. The Coulomb barriers have been calculated using the formulas of Refs. [10,32]. A reduction procedure was also applied to the cross sections which were divided by $(A_1^{1/3} + A_2^{1/3})$ for each corresponding system. This scaling takes into account geometrical effects in the magnitude of the cross sections due to different system radii. In the case of direct reactions, it is expected the cross sections to scale with a ring rather than a disk area, as in the case of total reaction cross sections. The ring area is given by: $\sigma \propto 2\pi Ra$ where R is the system radius and $a$ is a length parameter related to the diffuseness of the system. Here, we consider $a$ as a constant. This scaling method was suggested by Hussein in [56].

We observe in Fig. 18 that the reduced alpha cross sections for the $^{6}$He exotic projectile are considerably larger than the stable $^{6}$Li ones. This indicates that neutron transfers/breakup reactions are enhanced in collisions with $^{6}$He. It is interesting to mention that, in the reduced plot, the data for the $^{6}$Li+$^{208}$Pb system are falling along the same line as the lighter stable systems despite their very different masses showing that the reduction is working well.

### 4.2 First steps to particle-gamma coincidence measurements in RIBRAS

Usually, a large number of reaction channels are open in collisions induced by exotic projectiles. Due to their low binding energies, large deformations and large spectroscopic factors

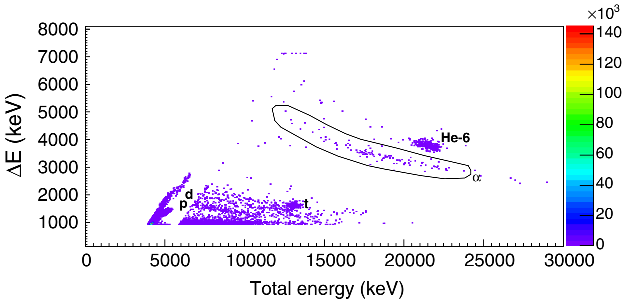

**Fig. 15** Two-dimensional $\Delta$E–E spectrum of the $^{6}$He +$^{120}$ Sn scattering at $E_{\rm lab}$=22.2 MeV and $\theta_{\rm lab}$=36° in scattering chamber 3. Figure taken from Ref. [48]

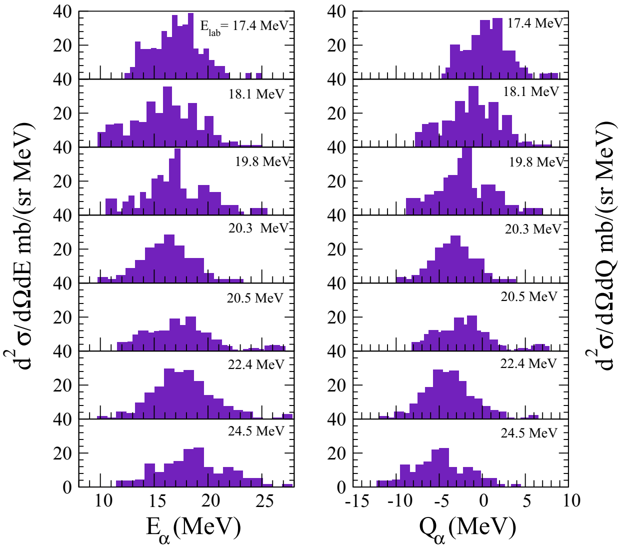

**Fig. 16** Energy and Q-distributions of the alpha particles from the $^{120}$Sn($^6$He,$\alpha$)$X$ reaction. Figure taken from Ref. [48]

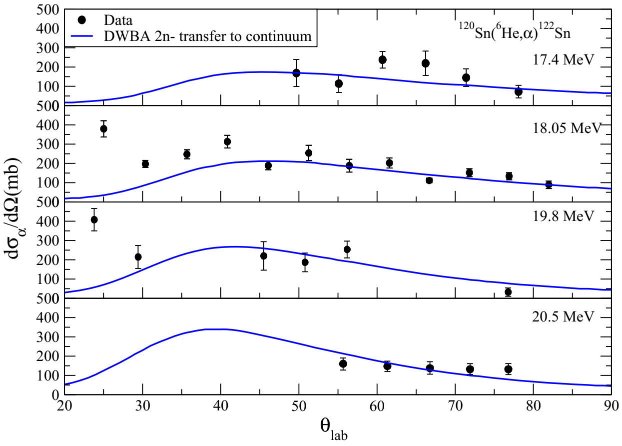

**Fig. 17** $^{120}$Sn($^6$He,$\alpha$)$X$ reaction angular distributions. The solid curves are 2n-transfer to continuum DWBA calculation from Ref. [5] normalized to reproduce the data

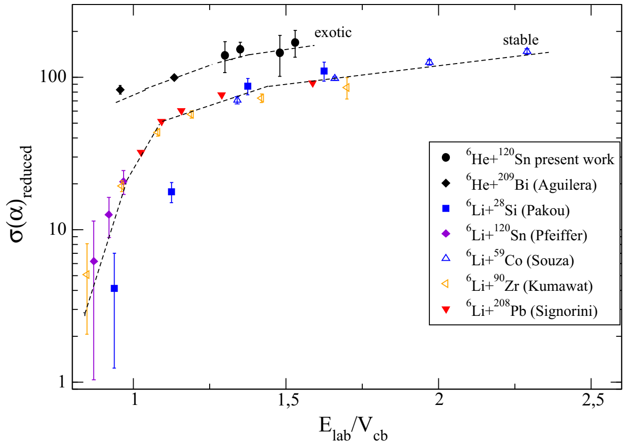

**Fig. 18** Reduced total alpha-particle cross sections from the $^{120}$Sn($^6$He, $\alpha$) reaction obtained from the angular distributions of Fig. 17 (black dots). See text for details on the reduction procedure. Black diamonds are data for the $^6$He+$^{209}$Bi system from Ref. [55]. Dashed lines are guides

for certain configurations, inelastic scattering, particle transfers, breakup and incomplete fusion reactions are enhanced even at low energies. The identification of reaction mechanisms other than elastic scattering requires the measurement of additional degrees of freedom such as neutrons and gammas.

In this section, the initial steps towards the implementation of a particle-$\gamma$ coincidence technique in RIBRAS and the results of a preliminary Coulomb excitation (Coulex) experiment on the $^8$Li+$^{120}$Sn system are outlined.

Coulex is one of the most interesting reaction channels for $\gamma$-particle coincident experiments. Former Coulex experiments with $^8$Li indicate a rather large quadrupole excitation probability [57], which is difficult to be understood in the light of nuclear structure models [58].

The Gamma-particle coincidence technique would provide a more stringent measurement of the $^8$Li excitation probability and it has motivated us to perform some experiments using the RIBRAS $^8$Li secondary beam. However, the RIBRAS system has some features, such as the high fringe magnetic field around its solenoids and a significant production of secondary neutrons in the primary target which impose limitations to the experiments and detectors that can be used.

For instance, proportional gas detectors, ionization chambers or the old photo-multipliers have their uses extremely limited at RIBRAS. The residual magnetic field of the solenoids can reach hundreds of Gauss in the region of the scattering chambers which practically prevents the operation of detectors based on slow electrons collection. In addition, the fast neutrons flux produced in the primary target in the forward direction has the potential to damage the Ge(Li) and Ge(HP) crystals, preventing their use as gamma detectors.

Newer types of crystals, such as the LYSO(Ce) [59], which are very efficient as gamma and X-ray detectors and are not critically damaged by neutrons. However, LYSO(Ce) crystals have an intrinsic radioactivity around 300 counts/cm$^3$/s [60] from the $^{176}$Lu $\beta$ decay. This radioactive background can contribute to random coincidences, eventually imposing some limitations to experiments.

A preliminary experiment was conducted in RIBRAS with a $^8$Li beam produced at 19.5 MeV and 22 MeV ($V_{cb}^{lab} = 20.5$ MeV) on a 3.8 mg/cm$^2$ $^{120}$Sn target. The secondary beam was filtered out by the two solenoids in cross over mode and focused in scattering chamber 3.

Four LYSO(Ce) detectors (model J-60035-4P-BGA) coupled to SiPM (silicon photo multiplier) [61]: $4 \times 4 - 3.8$ mm$^2$ for each pixel were mounted in scattering chamber 3 to detect the gammas. Two LYSO configurations were employed; in the first, the LYSO crystals 1 and 2 were rectangular parallelograms shaped with a 12.4 mm$^2$ square cross-section and 4 cm length; and, in the second one - LYSO 3 and 4: 16.0 mm$^2$ × 5 cm. Those detectors were positioned at the following distances from the secondary target: 3.2 cm; 3.5 cm; 4.1 cm; and 3.1 cm, respectively. With this setup, an overall gamma detection efficiency of about 1.5% was estimated using GEANT4 taking into account the actual geometry of this arrangement and the LYSO(Ce) photo-peak efficiency.

Three single silicon detectors and a $\Delta$E–E telescope were mounted in a support with the 4 detectors pointing towards the target at 20° with respect to the beam direction.

Timing between the particle and gamma signals was measured by a TDC (16 channels -Phillips-7186) triggered by the particle signals within a range of 200 ns.

Coincidence events were observed between gammas and particles in the silicon detectors. Few gammas were observed around the expected $^8$Li decay energy (980 keV), in coincidence with $^8$Li particles. However, the number of coincidences is still larger than expected from true Coulomb excitation events and seems to be more consistent with the expected number of random coincidences between the elastic $^8$Li peak and the intrinsic detector radioactivity.

As a preliminary conclusion from this experiment, we can say that the LYSO(Ce) gamma detectors seem to work well in the RIBRAS environment, but they present a large background of events that can not be completely eliminated by the gamma-particle coincidence condition. It is expected that with a better particle energy resolution and measurements at larger scattering angles, where the proportion of elastic to inelastic is not so large, this background would be under control. In a next round of experiments, it is planned to significantly increase $\gamma$-detection efficiency by increasing the number of LYSO crystals.

## 5 Conclusions

A review of the recent and some of the previous RIBRAS activity is presented. Elastic scattering angular distributions of $^6$He, $^7$Be, and $^8$B on several targets have been measured and analyzed by several models. The analysis includes Optical Model and CDCC calculations considering the effect of the projectile breakup on the elastic angular distributions. For the $^6$He case, 4b-CDCC calculations reproduce quite well the elastic angular distributions for heavy ($^{120}$Sn), intermediate ($^{58}$Ni) and light ($^9$Be) mass targets, without parameter adjustments.

The total reaction cross sections obtained from those analyses have been reduced and compared with cros sections from stable weakly bound and tightly bound projectile systems showing an increasing pattern from tightly, to weakly bound and finally to the $^6$He and $^8$B exotic projectiles, the two latter presenting the largest reduced cross sections.

Non-elastic reaction channels such as alpha-particle production in the $^6$He $+^{120}$ Sn collision via the inclusive $^{120}$Sn($^6$He,$\alpha$)X reaction show large yields with differential cross sections in the range of hundreds of millibarns. The angle integrated alpha-particle cross-sections of $^6$He induced reactions are of the order of 1 barn, considerably larger than those obtained in other systems with the $^6$Li projectile.

In summary, low energy elastic scattering and transfer reaction measurements of exotic projectiles show a large total reaction cross section in comparison with similar stable systems. The coupling to the projectile breakup channel explains well the elastic angular distributions but not the projectile fragment distributions, which are largely underestimated by the CDCC calculations. In the case of the $^6$He induced reactions, DWBA transfer to continuum calculations provide results in better agreement with the observed alpha particle yields, indicating that at low energies, neutron transfers can play an important role in the reaction mechanism.

**Acknowledgements** This work has been partially supported by Conselho Nacional de Desenvolvimento Científico e Tecnológico – CNPq (Brazil), Fundação de Amparo à Pesquisa do Estado de São Paulo, FAPESP (Brazil), contracts no. 2019/02759-0, 2019/07767-1, Coordenação de Aperfeiçoamento de Pessoal de Nível Superior – Brasil (CAPES) – Finance Code 88887.355019/2019, and Fundação de Amparo à Pesquisa do Estado do Rio de Janeiro, FAPERJ (Brazil). We would like to thank Prof. M. Moralles for the availability of Calor3.0 code used for GEANT4 evaluations of $\gamma$ detection efficiencies. We would like to thank Prof. W Seale for careful reading and valuable suggestions to the text of this article.

**Data Availability Statement** This manuscript has associated data in a data deposited. [Authors' comment: This manuscript has associated data in data repositories, EXFOR and http://nrv.jinr.ru/nrv/webnrv/elastic_scattering/reactions.php, or upon request by contacting the corresponding author.]

## References

1. R. Lichtenthäler, A. Lépine-Szily, V. Guimarães, C. Perego, V. Placco, O. Camargo jr., R. Denke, P. N. de Faria, E. A. Benjamim, N. Added, G. F. Lima, M. S. Hussein, J. Kolata, A. Arazi, Radioactive Ion beams in Brazil (RIBRAS), Eur. Phys. J. A 25 (2005) 733. https://doi.org/10.1140/epjad/i2005-06-043-y
2. A. Lépine-Szily, R. Lichtenthäler, V. Guimarães, The radioactive ion beams in Brazil (RIBRAS) facility. Eur. Phys. J. A **50**, 128 (2014). https://doi.org/10.1140/epja/i2014-14128-4
3. R. Lichtenthäler, M.A.G. Alvarez, A. Lépine-Szily, S. Appannababu, K.C.C. Pires, U.U. da Silva, V. Scarduelli, R.P. Condori, N. Deshmukh, RIBRAS: the facility for exotic nuclei in Brazil. Few Body Syst. **57**, 157–163 (2016). https://doi.org/10.1007/s00601-015-1039-z
4. E. Benjamim, A. Lépine-Szily, D. Mendes Junior, R. Lichtenthöler, V. Guimarães, P. Gomes, L. Chamon, M. Hussein, A. Moro, A. Arazi, I. Padron, J. Alcantara Nuñez, M. Assunção, A. Barioni, O. Camargo, R. Denke, P. de Faria, K. Pires, Elastic scattering and total reaction cross section for the $^6$He + $^{27}$Al system, Phys. Lett. B 647 (1) (2007) 30 – 35. https://doi.org/10.1016/j.physletb.2007.01.048
5. P.N. de Faria, R. Lichtenthäler, K.C.C. Pires, A.M. Moro, A. Lépine-Szily, V. Guimarães, D.R. Mendes Jr., A. Arazi, A. Barioni, V. Morcelle, M.C. Morais, $\alpha$-particle production in $^6$He $+^{120}$ Sn collisions. Phys. Rev. C **82**(3), 034602 (2010). https://doi.org/10.1103/PhysRevC.82.034602
6. P. N. de Faria, R. Lichtenthäler, K. C. C. Pires, A. M. Moro, A. Lépine-Szily, V. Guimarães, D. R. Mendes jr., A. Arazi, M. Rodríguez-Gallardo, A. Barioni, V. Morcelle, M. C. Morais, O. Camargo, J. Alcantara Nuñez, M. Assunção, Elastic scattering and total reaction cross section of $^6$He $+^{120}$ Sn, Phys. Rev. C 81 (2010) 044605. https://doi.org/10.1103/PhysRevC.81.044605
7. P. Mohr, P.N. de Faria, R. Lichtenthäler, K.C.C. Pires, V. Guimarães, A. Lépine-Szily, D.R. Mendes, A. Arazi, A. Barioni, V. Morcelle, M.C. Morais, Comparison of $^{120}$Sn($^6$He,$^6$ He)$^{120}$Sn and $^{120}$Sn($\alpha,\alpha$)$^{120}$Sn elastic scattering and signatures of the $^6$He neutron halo in the optical potential. Phys. Rev. C **82**, 044606 (2010). https://doi.org/10.1103/PhysRevC.82.044606
8. V. Morcelle, R. Lichtenthäler, A. Lépine-Szily, V. Guimarãaes, K. C. C. Pires, J. Lubian, D. R. Mendes Junior, P. N. de Faria, J. J. Kolata, F. D. Becchetti, H. Jiang, E. F. Aguilera, D. Lizcano, E. Martinez-Quiroz, H. Garcia, $^8$B + $^{27}$Al scattering at low energies, Phys. Rev. C 95 (2017) 014615. https://doi.org/10.1103/PhysRevC.95.014615
9. V. Morcelle, R. Lichtenthäler, R. Linares, M. C. Morais, V. Guimarães, A. Lépine-Szily, P. R. S. Gomes, J. Lubian, D. R. Mendes Junior, P. N. De Faria, A. Barioni, L. R. Gasques, J. M. B. Shorto, K. C. C. Pires, J. C. Zamora, R. P. Condori, V. Scarduelli, J. J. Kolata, H. Amro, F. D. Becchetti, H. Jiang, E. F. Aguilera, D. Lizcano, E. Martinez-Quiroz, H. Garcia, Elastic scattering and total reaction cross section for the $^7$Be + $^{27}$Al system at near-barrier energies, Phys. Rev. C 89 (2014) 044611. https://doi.org/10.1103/PhysRevC.89.044611
10. K.C.C. Pires, S. Appannababu, R. Lichtenthäler, O.C.B. Santos, New method to calculate the nuclear radius from low energy fusion and total reaction cross sections. Phys. Rev. C **98**, 014614 (2018). https://doi.org/10.1103/PhysRevC.98.014614
11. K. C. C. Pires, R. Lichtenthäler, A. Lépine-Szily, V. Guimarães, P. N. de Faria, A. Barioni, D. R. Mendes Junior, V. Morcelle, R. Pampa Condori, M. C. Morais, J. C. Zamora, E. Crema, A. M. Moro, M. Rodríguez-Gallardo, M. Assunção, J. M. B. Shorto, S. Mukherjee, Experimental study of $^6$He $+^9$ Be elastic scattering at low energies, Phys. Rev. C 83 (2011) 064603. https://doi.org/10.1103/PhysRevC.83.064603
12. K.C.C. Pires, R. Lichtenthäler, A. Lépine-Szily, V. Morcelle, Total reaction cross section for the $^6$He $+^9$ Be system. Phys. Rev. C **90**, 027605 (2014). https://doi.org/10.1103/PhysRevC.90.027605
13. U. Umbelino, K.C.C. Pires, R. Lichtenthäler, V. Scarduelli, G.A. Scotton, A. Lépine-Szily, V. Guimarães, J. Lubian, B. Paes, J.L. Ferreira, M.A.G. Alvarez, J.M.B. Shorto, S. Appannababu, M. Assunção, R.P. Condori, V. Morcelle, Two-neutron transfer in $^7$Be $+^9$ Be collisions. Phys. Rev. C **99**, 064617 (2019). https://doi.org/10.1103/PhysRevC.99.064617
14. V. Morcelle, K. C. C. Pires, M. Rodríguez-Gallardo, R. Lichtenthäler, A. Lépine-Szily, V. Guimarães, P. N. Faria, D. R. Mendes Junior, A. M. Moro, L. R. Gasques, E. Leistenschneider, R. Pampa Condori, V. Scarduelli, M. C. Morais, A. Barioni, J. C. Zamora, J. M. B. Shorto, Four-body effects in the $^6$He $+^{58}$ Ni scattering, Phys. Lett. B 732 (2014) 228. https://doi.org/10.1016/j.physletb.2014.03.043
15. O. C. B. Santos, PhD thesis, Instituto de Física da USP 2021
16. U. Umbelino, PhD thesis, Instituto de Física da USP 2021
17. F.D. Bechetti, M.Y. Lee, T.W. O'Donnell, D.A. Roberts, J.J. Kolata, L.O. Lamm, G. Rogachev, V. Guimaraes, P.A. DeYoung, S. Vincent, Nucl. Instrum. Methods Phys. Res. A **505**, 377 (2003)
18. D. Yamaguchi, H. an d Kahl, S. Kubono, Crib: the low energy in-flight ri beam separator, Nucl. Phys. News Int. 30 (2020) 21–27
19. V. Z. Maidikov, et al., Nucl. Phys. A 389c (2004) 746
20. F. Farinon et al., NIM B **266**, 4097 (2008)
21. M. Mazzocco et al., NIM B **266**, 4665 (2008)
22. M. Mazzocco et al., NIM B **317**, 223 (2013)
23. A. Villari et al., Nucl. Phys. A **787**, 126c–133c (2007)
24. G. Ball, L. Buchmann, B. Davids, R. Kanungo, C. Ruiz, C.E. Svensson, J. Phys. G **38**, 024003 (2011)
25. J. P. Fernandez-Garcia, M. Cubero, M. Rodriguez-Gallardo, L. Acosta, M. Alcorta, M. A. G. Alvarez, M. J. G. Borge, L. Buchmann, C. A. Diget, H. A. Falou, B. R. Fulton, H. O. U. Fynbo, D. Galaviz, J. Gomez-Camacho, R. Kanungo, J. A. Lay, M. Madurga, I. Martel, A. M. Moro, I. Mukha, T. Nilsson, A. M. Sanchez-Benitez, A. Shotter, O. Tengblad, P. Walden, $^{11}$Li Breakup on $^{208}$Pb at energies around the coulomb barrier, Phys. Rev. Lett. 110 (14). https://doi.org/10.1103/PhysRevLett.110.142701
26. J. Xia, W. Zhan, B. Wei, Y. Yuan, M. Song, W. Zhang, X. Yang, P. Yuan, D. Gao, H. Zhao, X. Yang, G. Xiao, K. Man, J. Dang, X. Cai, Y. Wang, J. Tang, W. Qiao, Y. Rao, Y. He, L. Mao, Z. Zhou, The heavy ion cooler-storage-ring project (hirfl-csr) at lanzhou, Nucl. Instrum. Meth- ods Phys. Res., Sect. A, Accel. Spectrom. Detect. Assoc. Equip. 488 (1) (2002) 11–25. https://doi.org/10.1016/S0168-9002(02)00475-8, http://www.sciencedirect.com/science/article/pii/S0168900202004758
27. F.F. Duan et al., Phys. Lett. B **811**, 135942 (2020)
28. D.R. Tilley et al., Nucl. Phys. A **708**, 3 (2002)
29. A.M. Moro, K. Rusek, J.M. Arias, J. Gomez-Camacho, M. Rodriguez-Gallardo, Improved di-neutron cluster model for $^6$He scattering. Phys. Rev. C **75**, 064607 (2007). https://doi.org/10.1103/PhysRevC.75.064607
30. M. Rodriguez-Gallardo, J. M. Arias, J. Gomez-Camacho, R. C. Johnson, A. M. Moro, I. J. Thompson, J. A. Tostevin, Four-body continuum-discretized coupled-channels calculations using a transformed harmonic oscillator basis, Phys. Rev. C 77 (6). https://doi.org/10.1103/PhysRevC.77.064609
31. M. Rodriguez-Gallardo, J.M. Arias, J. Gomez-Camacho, A.M. Moro, I.J. Thompson, J.A. Tostevin, Four-body continuum-discretized coupled-channels calculations. Phys. Rev. C **80**(5), 051601(R) (2009). https://doi.org/10.1103/PhysRevC.80.051601
32. A.S. Freitas, L. Marques, X.X. Zhang, M.A. Luzio, P. Guillaumon, R.P. Condori, R. Lichtenthäler, Woods–Saxon equivalent to a double folding potential. Braz. J. Phys. **46**, 120 (2016). https://doi.org/10.1007/s13538-015-0387-y
33. R.B. Taylor, N.R. Fletcher, R. Davis, Nucl. Phys. **65**, 318 (1965)

34. J.H. Dave, C.R. Gould, Phys. Rev. C **28**, 2212 (1983)
35. C. Perey, F. Perey, Compilation of phenomenological optical-model parameters 1954–1975. Atomic Data Nucl. Data Tables **17**(1), 1–101 (1976). https://doi.org/10.1016/0092-640X(76)90007-3
36. P.R.S. Gomes et al., Phys. Lett. B **601**, 20 (2004)
37. L. C. Chamon, B. V. Carlson, L. R. Gasques, D. Pereira, C. De Conti, M. A. G. Alvarez, M. S. Hussein, M. A. Cândido Ribeiro, E. S. Rossi, C. P. Silva, Toward a global description of the nucleus-nucleus interaction, Phys. Rev. C 66 (2002) 014610. https://doi.org/10.1103/PhysRevC.66.014610
38. S. Verma, *et al.*, EPJA44,385(2010)
39. M.J. Ermamatov et al., Phys. Rev. C **94**, 024610 (2016)
40. D. Pereira, J. Lubian, J.R.B. Oliveira, D.P. de Sousa, L.C. Chamon, An imaginary potential with universal normalization for dissipative processes in heavy-ion reactions. Phys. Lett. B **670**(4), 330–335 (2009). https://doi.org/10.1016/j.physletb.2008.10.066
41. M. Avrigeanu et al., At. Data Nucl. Data Tables **95**, 501 (2009)
42. B.A. Watson, P. Singh, R. Segel, Phys. Rev. **182**, 977 (1969)
43. A.J. Koning, J.P. Delaroche, Nucl. Phys. A **713**, 231 (2003)
44. V. Avrigeanu, P.E. Hodgson, M. Avrigeanu, Phys. Rev. C **49**, 2136 (1994)
45. A. Pakou et al., Phys. Rev. C **87**, 014619 (2013)
46. M. Cubero, J. P. Fernandez-Garcia, M. Rodriguez-Gallardo, L. Acosta, M. Alcorta, M. A. G. Alvarez, M. J. G. Borge, L. Buchmann, C. A. Diget, H. Al Falou, B. R. Fulton, H. O. U. Fynbo, D. Galaviz, J. Gomez-Camacho, R. Kanungo, J. A. Lay, M. Madurga, I. Martel, A. M. Moro, I. Mukha, T. Nilsson, A. M. Sanchez-Benitez, A. Shotter, O. Tengblad, P. Walden, Do halo nuclei follow rutherford elastic scattering at energies below the barrier? The case of $^{11}$Li, Phys. Rev. Lett. 109 (26). https://doi.org/10.1103/PhysRevLett.109.262701
47. A. Arazi, J. Casal, M. Rodriguez-Gallardo, J. M. Arias, R. Lichtenthaeler Filho, D. Abriola, O. A. Capurro, M. A. Cardona, P. F. F. Carnelli, E. de Barbara, J. Fernandez Niello, J. M. Figueira, L. Fimiani, D. Hojman, G. V. Marti, D. Martinez Heimman, A. J. Pacheco, $^{9}$Be+$^{120}$Sn scattering at near-barrier energies within a four-body model, Phys. Rev. C 97 (4). https://doi.org/10.1103/PhysRevC.97.044609
48. S. Appannababu, R. Lichtenthäler, M.A.G. Alvarez, M. Rodríguez-Gallardo, A. Lépine-Szily, K.C.C. Pires, O.C.B. Santos, U.U. Silva, P.N. de Faria, V. Guimarães, E.O.N. Zevallos, V. Scarduelli, M. Assunção, J.M.B. Shorto, A. Barioni, J. Alcántara-Núñez, V. Morcelle, Two-neutron transfer in the $^{6}$He + $^{120}$Sn reaction. Phys. Rev. C **99**, 014601 (2019). https://doi.org/10.1103/PhysRevC.99.014601
49. R. Lichtenthaler, S. Appannababu, *et. al.*, Alpha-particle production in the $^{6}$He+$^{120}$Sn collision., INPC-19 proceedings
50. K. O. Pfeiffer, E. Speth, B. K., Nucl. Phys. A 206 (1973) 545–557
51. A. Pakou, N. Alamanos, A. Gillibert, M. Kokkoris, S. Kossionides, A. Lagoyannis, N. G. Nicolis, G. Papachristodoulou, D. Patiris, D. Pierroutsakou, E. C. Pollacco, R. K., Phys. Rev. Lett. 90, 202701-1 (2003)
52. H. Kumawat et al., Phys. Rev. C **81**, 054601 (2010)
53. F.A. Souza et al., Nucl. Phys. A **821**, 36 (2009)
54. C. Signorini et al., Eur. Phys. J. A **10**, 249–253 (2001)
55. E.F. Aguilera et al., Phys. Rev. Lett. **84**, 5058 (2000)
56. M.S. Hussein, R. Lichtenthäler, F.M. Nunes, I.J. Thompson, Scaling and interference in the dissociation of halo nuclei. Phys. Lett. B **640**(3), 91–95 (2006). https://doi.org/10.1016/j.physletb.2006.07.046
57. J.A. Brown, F.D. Becchetti, J.W. Jänecke, K. Ashktorab, D.A. Roberts, J.J. Kolata, R.J. Smith, K. Lamkin, R.E. Warner, Coulomb excitation of $^{8}$Li. Phys. Rev. Lett. **66**, 2452–2455 (1991)
58. A. Umeya, K. Muto, Shell model study on e2 effective charges in light neutron-rich nuclei. Nucl. Phys. A **722**, C558–C562 (2003). https://doi.org/10.1016/S0375-9474(03)01427-1
59. P. Eckert et al., Characterisation studies of silicon photomultipliers. Nucl. Instrum. Methods Phys. Res. A **620**, 217–226 (2010)
60. H. Alva-Sáinchez, *et al.*, Sci. Rep. (2018) 8:17310 https://doi.org/10.1038/s41598-018-35684-x
61. http://www.onsemi.com/sensors